Multiresolution Models of DC Traction Power Supply Systems With Reversible Substations

Fulin Fan, Yafang Li, Smail Ziani, Brian G Stewart

Wiley
IET Electrical Systems in Transportation
Volume 2024, Article ID 8279648, 19 pages
https://doi.org/10.1049/2024/8279648

The Institution of Engineering and Technology | WILEY

Research Article

Multiresolution Models of DC Traction Power Supply Systems With Reversible Substations

Fulin Fan,[1,2] **Yafang Li**,[3] **Smail Ziani**,[4] **and Brian G. Stewart**[2]

[1]*School of Electrical Engineering and Automation, Harbin Institute of Technology, Harbin 150001, China*
[2]*Institute for Energy and Environment, University of Strathclyde, Glasgow, G1 1XW, UK*
[3]*Hitachi Energy, Ludvika 771 31, Sweden*
[4]*IRT Railenium, Valenciennes, Famars 59540, France*

Correspondence should be addressed to Fulin Fan; fulin.fan@hit.edu.cn

Received 13 October 2023; Revised 19 July 2024; Accepted 1 September 2024

Academic Editor: Jagabar Sathik

Reversible substations (RSs) permitting bidirectional power flows can recover the regenerative braking energy of trains in DC traction power supply systems (TPSSs), increasing the energy efficiency of railway systems. To predict their effects on system dynamics and energy savings, the paper develops multiresolution models (MRMs) to simulate the RS roles with different fidelities. A high-resolution model for the transient simulation replicates a particular topology where a three-level voltage source inverter is connected to the secondary winding of an existing 12-pulse rectifier transformer and regulated to keep a constant DC voltage in the inverting mode. Furthermore, it can model the transient effects of pantograph-to-line arcing by inserting arc voltage profiles at the train's input stage. To increase the computation speed in the long-term energy flow simulation, a low-resolution model simplifies the rectifiers into a series connection of a diode and a controlled voltage source depicting their nonlinear output characteristics and then places a DC voltage source in parallel to form a reverse path for braking power recovery. In addition, nonlinear conversion efficiencies are introduced to calculate energy flows across substations. The MRMs are tested based on a 1.5 kV DC TPSS and discussed alongside system dynamics under normal operation or pantograph arcing and the consistencies between different models. The RS using bidirectional voltage source converters only is additionally modelled to compare the technical performance of the two topologies in terms of system dynamics and energy efficiencies.

1. Introduction

In the transition to low-carbon energy systems, European railway systems are required to improve the energy efficiency in order to cut 30% of their final energy usage and 50% of average CO_2 emissions from train operations by 2030 compared to the base year 1990 [1]. The majority of published approaches to improving the energy efficiency of DC traction power supply systems (TPSSs) deal with an efficient management of the regenerative braking energy of trains [2, 3]. The regenerated energy cannot only be used by on-board auxiliary systems but also be delivered to surrounding trains for their consumption via overhead lines (OHLs or third rails) subject to OHL voltage limits. The excess braking energy that cannot be recovered will be dissipated as heat in on-board dumping resistors so as to avoid violation of the overvoltage limit [2]. The braking energy recovery can be improved by synchronising the acceleration and deceleration of neighbouring trains and/or injecting the excess braking energy into stationary or on-board energy storage devices (ESDs) [2, 3]. Reversible substations (RSs) provide another efficient recovery method through feeding the braking power to AC sides which can be used by AC equipment in RSs or even sold back to electricity suppliers subject to legislations and rules of local networks [3, 4]. Compared to ESDs, RSs are expected to have lower safety issues and reduce energy conversion losses [4].

A traditional unidirectional substation (US) at a DC TPSS can be upgraded to an RS either by placing an inverter in antiparallel with the existing rectifiers or through a direct replacement of the rectifiers with a bidirectional converter [2, 3]. Because of the costly investment in RSs, it is necessary

to evaluate the energy savings and associated benefits before their deployment [5]. This requires the TPSS-level energy flow simulation to quantify the energy exchange between DC and AC sides during a long period of interest (e.g. from minutes [5–10] to hours [11–13]). The long-term simulation is usually implemented at a relatively low resolution (e.g. 1-s intervals [9–11, 14]) by using the current injection method [7–9, 11] or the Newton–Raphson method [13, 14] so as to increase computation speeds but at the expense of a reduced accuracy. The TPSS-level simulation of energy flows and voltage profiles not only permits evaluating the RS benefits at a planning stage [11, 15, 16] but can also assist in optimising the RS's operating characteristics [8, 14] or its coordination with ESDs [11].

In addition to the energy-saving estimation, voltage and current (V-I) transients at an RS must be modelled in advance to examine the effectiveness of the RS control method to be applied and its impacts on device stress, power quality and system stability [11, 17]. This focuses more on the converter-level simulation that replicates actual converter topologies and runs at a sufficiently high resolution (e.g. 5-μs intervals [6, 11, 18] or even shorter [17]) to ensure the accuracy of the V-I dynamics modelled within a short period of interest. Given a direct replacement of USs with bidirectional converters, reference [11] or [17] simulates two-level four-quadrant and modular multilevel converters, respectively, that are controlled to maintain the DC voltage constantly at a specific level subject to their capacity. Instead of a constant DC voltage control, a droop control linearly reducing the voltage reference level with the converter export is explored in [19] and [20]. Some research has also been devoted to coordinating the existing rectifiers and their antiparallel voltage source converter (VSC) or voltage source inverter (VSI). The VSI is generally switched off when an RS is in rectifying modes and activated in inverting modes when the DC voltage across the RS exceeds a predefined reference level due to the injection of excess braking current into the OHL [6, 18]. In [21] and [22], the VSCs additionally assist rectifiers in the DC power supply by sharing traction loads during rectifying modes. However, the antiparallel VSI or VSC in these research is directly connected to the main AC grid rather than by using the existing three-winding transformer of a 12-pulse diode rectifier which can reduce the RS investment in practice.

To permit evaluating V-I dynamics and energy savings of a DC TPSS with an RS, this paper develops multiresolution models (MRMs) for the converter-level and TPSS-level simulations. The MRMs simulate a particular RS topology that links an antiparallel VSI to a secondary winding of the existing three-winding rectifier transformer, forming the path for braking power recovery only. This reduces the capacity requirement on the new equipment set compared to the use of bidirectional VSCs that must additionally supply the greater electricity consumptions of trains, thus permitting a more economical way of upgrading a US to an RS. Instead of the traditional two-level VSI or VSC studied in [8, 11, 14] and [20–22], the high-resolution model (HRM) is developed here based on a three-level active neutral point clamped (ANPC) VSI due to its reduced harmonic injection and improved distributions of stress and losses across switching devices [23]. The ANPC VSI works in the inverting mode only and maintains a constant DC voltage for an improved system receptivity for braking energy [20]. In addition to the normal train operation that has been widely modelled in existing literature, the HRM enables the simulation of system transients in pantograph-to-OHL arc events by inserting arc voltage profiles at the train's input stage, which allows analysing the effects of pantograph arcing on the RS operation. Then the paper proposes a novel simplified representation for the antiparallel connection of the diode rectifier and the VSI which forms the basis of the low-resolution model (LRM). The function of a rectifier is realised by a diode in series with a controlled voltage source (CVS) that reflects its nonlinear output characteristic, while the ANPC VSI under the constant DC voltage control is simplified into a DC voltage source that is parallel connected with the CVS branch. Compared with most research using linear resistors to simulate overall voltage drops and energy losses in transformers and converters [7–16], the LRM developed here fully takes into account the nonlinearity that exists not only in the V-I relationship at rectifier outputs but also in the converter efficiencies, permitting a more realistic simulation of the RS operating characteristics. In addition to the antiparallel connection of the VSI with existing rectifiers, the RS development through an entire replacement of rectifiers with bidirectional ANPC VSCs is also simulated in this work to compare the influences of the two RS topologies on system dynamics and energy efficiencies.

The paper is structured as follows: Section 2 describes the HRM including the RS control method and the modelling of a train moving along an OHL with pantograph arc occurrences; Section 3 introduces the simplified converter representations in the LRM; Section 4 discusses the RS operation simulated in both normal operation and pantograph arc events and evaluates the LRM accuracy in energy flow simulation; and Section 5 presents conclusions and recommendations for further work.

2. HRM of DC Traction System

2.1. Converter Topologies at RS. A particular RS connecting an ANPC VSI in antiparallel with a 12-pulse diode rectifier is shown in Figure 1. The RS connects to an upstream 15 kV AC grid and supports the operation of a 1.5 kV DC TPSS. The VSI uses two pairs of insulated-gate bipolar transistors (IGBTs) per phase, with the midpoint of each pair being linked to the neutral point of the VSI through an additional IGBT [23]. When the DC voltage V_{RS} across the RS reaches a specific level $V_{VSI,act}$ of 1780 V due to the injection of surplus braking current into the OHL, the RS works in the inverting mode and activates the VSI to keep V_{RS} constantly at $V_{VSI,act}$ while exporting AC currents to a 1225 V/690 V transformer (TX) *B* whose primary winding (delta) is linked to the secondary winding (delta) of the upstream three-winding TX *A*. The two capacitors with a 30 mF equivalent capacitance *C* are placed at the DC side of the VSI to stabilise its input voltage, while an AC filter consisting of resistor R_f and

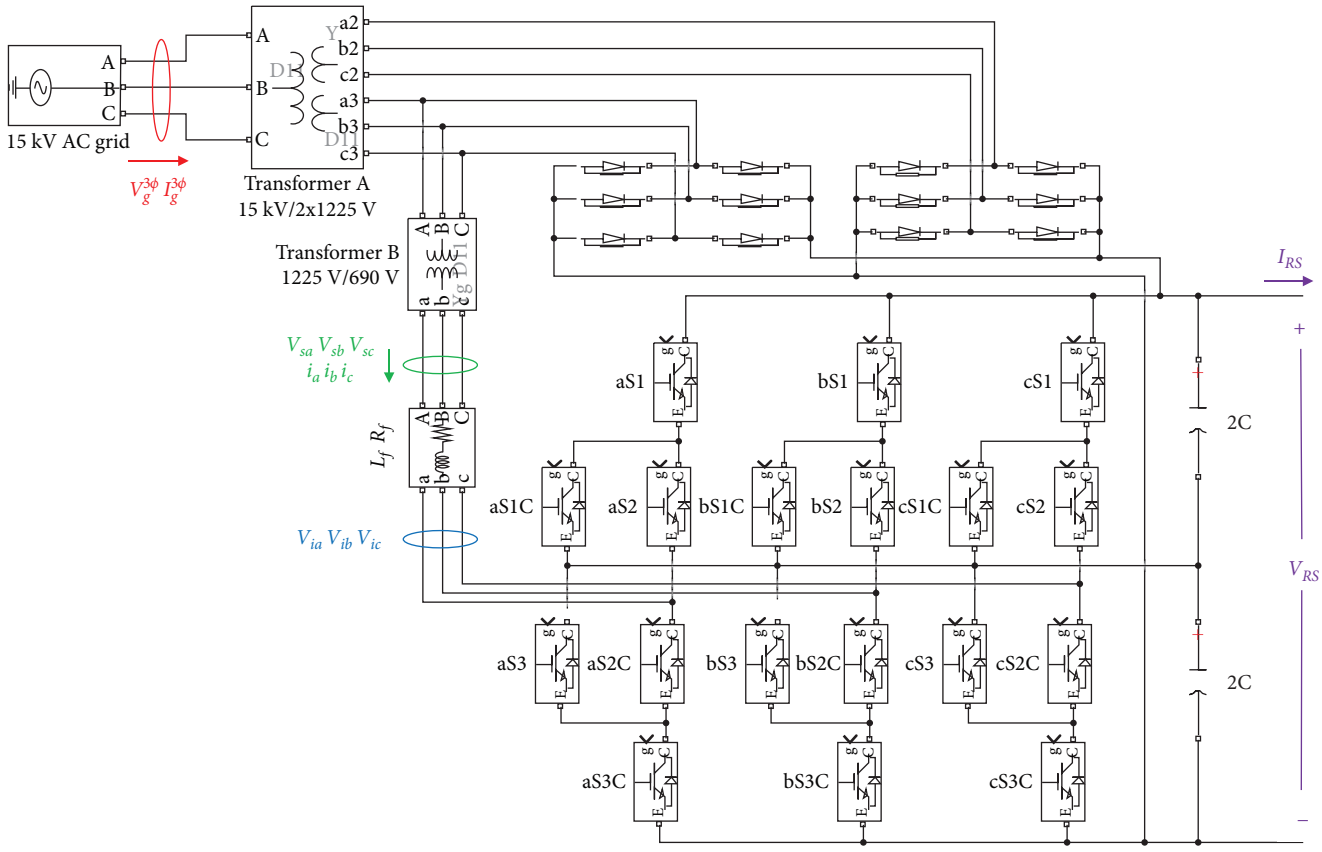

FIGURE 1: A particular RS topology consisting of a 12-pulse diode rectifier and an antiparallel ANPC VSI.

inductor L_f is placed between the VSI output and TX *B* to improve the power quality of the braking power fed to the AC side and reduce the stresses on TX and VSI components. When no braking current is transferred to the RS (i.e. $I_{RS} \geq 0$), the VSI will be deactivated by switching off all the IGBTs. In the traction mode, the three-winding TX *A* supplies two 1225 V three-phase AC voltages with a phase difference of 30° to two parallel connected six-pulse rectifiers [3]. The 12-pulse ripples in their output voltage are smoothed by the capacitors and then supplied to the train via an OHL. It is noted that the *C* value is carefully selected here to ensure the performance of the VSI in feeding braking current to the AC grid. The 30 mF *C* used here far exceeds the capacitance of the conventional LC filter for a US (hundreds of μF [24]) which thus has negligible effects on the DC output smoothing and is removed from the DC output of the rectifiers in this work.

Table 1 lists technical parameters of the RS simulated here. It is noted that the VSI activation voltage of 1780 V is set to be higher than the rectifier's no-load voltage (i.e. $\sqrt{2} \times 1225 \approx 1732.4$ V) in order to form a deadband for the transition between the two modes and avoid the current circulation between the VSI and the rectifier [25]. The AC power consumed or fed by the TPSS via the RS can be computed from the three-phase V-I (i.e. $V_g^{3\phi}$ and $I_g^{3\phi}$) measured at the AC grid. In practice, a US or an RS generally comprises two identical converting equipment sets that are parallel connected for an improved system capacity and reliability [11]. Figure 1 shows a single equipment set only for brevity.

TABLE 1: Technical parameters of the modelled RS.

Parameter	Value	Parameter	Value
TX A voltage	15 kV/2 × 1225 V	TX resistance	0.0065 p.u.
TX B voltage	1225 V/690 V	TX inductance	0.0571 p.u.
TX capacity	3.3 MVA	*C*	30 mF
R_f	2 mΩ [18]	L_f	0.25 mH [18]

To understand technical performance differences between the specific RS topology in Figure 1 and the RS topology that directly employs multiquadrant VSCs, V-I dynamics of a DC TPSS with an RS that replaces the entire diode rectifiers by ANPC VSCs, as shown in Figure 2, are additionally simulated in this work. Figure 2 shows a single equipment set for brevity, though the parallel connection of two identical ANPC VSCs is modelled here considering the system reliability requirement in practice. In this particular topology, the ANPC VSCs are designed to work for both rectifying and inverting, with the DC voltage V_{RS} being maintained at the same level as the no-load voltage of the diode rectifiers at other USs within the TPSS. The topologies in Figures 1 and 2 are denoted here by D + VSI-based and VSC-only-based ones, respectively.

2.2. Constant DC Voltage Control of ANPC VSI. As shown in Figures 1 and 2, the output voltage V_{ia}, V_{ib} and V_{ic} of the VSI or VSC can be calculated from the phase V-I (i.e. V_{sa}, V_{sb}, V_{sc},

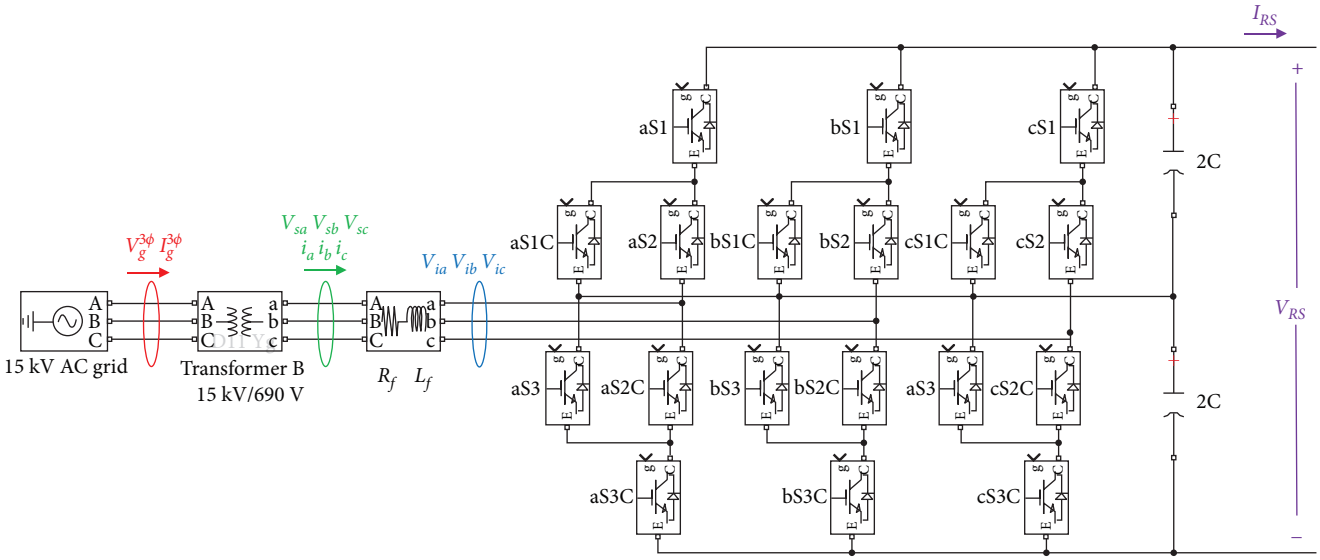

FIGURE 2: A particular RS topology comprising an ANPC VSC-only.

i_a, i_b and i_c) on the secondary side of TX B by using Equation (1):

$$\begin{cases} V_{ia} = V_{sa} - \left(R_f + L_f \cdot \dfrac{d}{dt}\right) \cdot i_a \\ V_{ib} = V_{sb} - \left(R_f + L_f \cdot \dfrac{d}{dt}\right) \cdot i_b \\ V_{ic} = V_{sc} - \left(R_f + L_f \cdot \dfrac{d}{dt}\right) \cdot i_c \end{cases}, \quad (1)$$

where R_f and L_f represent the filter resistance and inductance at the VSI or VSC output. Since the VSI or VSC control method generally requires constant quantities in the steady state and eliminating steady-state errors while using proportional integral (PI) controllers [26], the Clarke and Park transforms [27] are used to convert the V-I variables in Equation (1) that oscillate in the three-phase (abc) reference frame into a direct-quadrature-zero ($dq0$) rotating frame:

$$\begin{cases} V_{id} = V_{sd} - \left(R_f + L_f \cdot \dfrac{d}{dt}\right) \cdot i_d + w \cdot L_f \cdot i_q \\ V_{iq} = V_{sq} - \left(R_f + L_f \cdot \dfrac{d}{dt}\right) \cdot i_q - w \cdot L_f \cdot i_d \end{cases}, \quad (2)$$

where w is the angular frequency of the grid and the V-I variables with subscripts d and q denote their respective direct and quadrature components. When the VSI is activated to work in the inverting mode, a constant DC voltage control method will mitigate the deviation of the monitored V_{RS} from the reference $V_{VSI,act}$ by using a PI controller to produce a reference i_d^* for i_d while meeting the power balance of the VSI [20]. Figure 3 shows the constant DC voltage control scheme where V_{sd}^r is the rated value of V_{sd}. The constant DC voltage control scheme is also applied to the

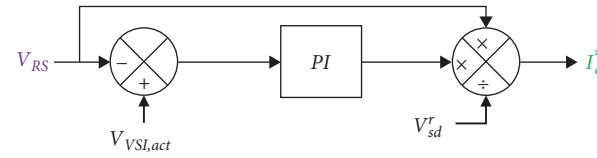

FIGURE 3: The scheme of the constant DC voltage control.

bidirectional VSCs for both rectifying and inverting modes, though the no-load voltage level of the diode rectifiers at other USs is adopted as the reference voltage for the monitored V_{RS}.

The reference of i_q (i.e. denoted by i_q^*) determining the reactive power output of the VSI or VSC is set to 0 in this work which enables the VSI or VSC to operate at a unity power factor [18]. The deviations of i_d and i_q from their respective i_d^* and i_q^* are then taken into two identical PI controllers to export the references V_{id}^* and V_{iq}^* for V_{id} and V_{iq}, respectively, based on Equation (2), forming an AC current control as shown in Figure 4. The PI parameters (K_P^D and K_I^D) for the constant DC voltage control or those (K_P^A and K_I^A) for the AC current control are determined by Equation (3) based on a damping factor $\xi = 0.707$ and the settling time of $t_s^D = 50$ ms or $t_s^A = 1$ ms, respectively, at which the second-order system is expected to reach the steady state within an acceptable error of $\varepsilon = 5\%$ [26]:

$$\begin{cases} K_P^D = 2 \cdot \xi \cdot C \cdot w_n^D \\ K_I^D = (w_n^D)^2 \cdot C \end{cases} \quad \begin{cases} K_P^A = 2 \cdot \xi \cdot L_f \cdot w_n^A - R_f \\ K_I^A = (w_n^A)^2 \cdot L_f \end{cases}, \quad (3)$$

where w_n^D or w_n^A denotes the natural frequency of the second-order system in the constant DC voltage or AC current control, respectively:

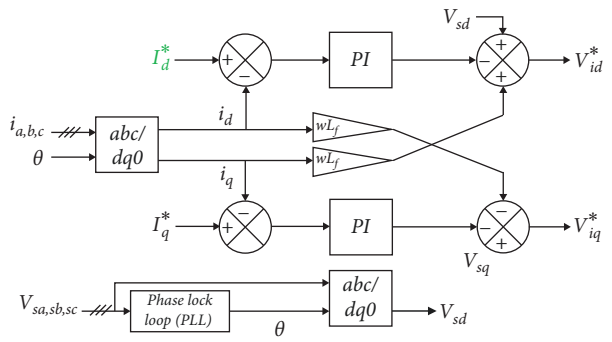

FIGURE 4: The scheme of the AC current control.

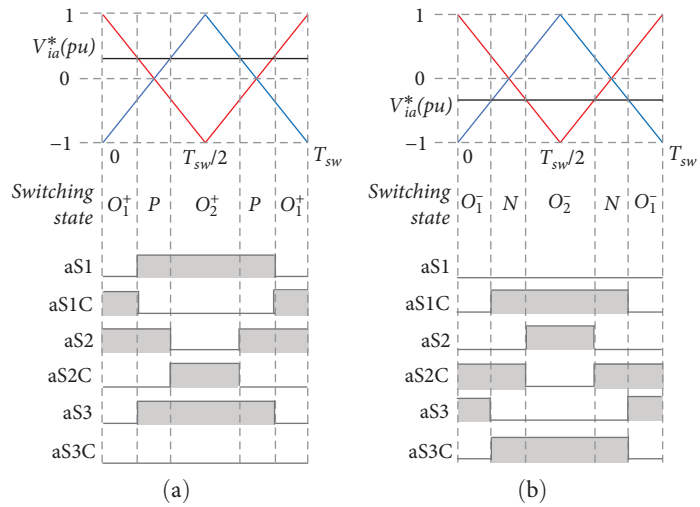

FIGURE 5: The PWM applied to an ANPC VSI or VSC with a switching frequency of 2 kHz for (a) positive or (b) negative phase voltage reference (in p.u.).

$$w_n^D = -\frac{\ln(\varepsilon)}{\xi \cdot t_s^D} \quad w_n^A = -\frac{\ln(\varepsilon)}{\xi \cdot t_s^A}. \tag{4}$$

Then V_{id}^* and V_{iq}^* in the *dq0* frame are converted into V_{ia}^*, V_{ib}^* and V_{ic}^* in the *abc* reference frame via the inverse Clarke and inverse Park transformation [27] so to instruct the IGBT states. This paper adopts a particular pulse width modulation (PWM) strategy for the ANPC VSI or VSC [28] which compares each phase voltage reference (in p.u.) with two carrier waves shifted by half of a switching period (i.e. $T_{sw}/2$) and then determines the on/off of the six IGBTs on that phase, as shown in Figure 5. This generates six switching states and results in a natural doubling of the apparent switching frequency [28].

2.3. Train and Lumped Parameter Line (LPL) Models. Since the paper focuses on the RS simulation, a train is simply modelled by connecting a controlled current source (CCS) in parallel with a resistive braking chopper which is modelled by a combination of 7.5 mF capacitor and 0.86 Ω braking rheostats and accompanied by a 100 μH smoothing inductor [29], as shown in Figure 6. The CCS is driven by the current I_{tr} consumed (+ve) or generated (−ve) by the train which is computed as the ratio of its electrical power to the measured voltage V_c across the CCS. The train power can be indirectly inferred from train properties and speed profiles based on vehicle dynamic equations [29] or directly calculated from on-board V-I measurements [30]. The braking resistors with an equivalent resistance of 0.86 Ω will start to absorb the excess braking energy when V_c increases beyond a specific level of 1930 V, avoiding the exceedance of the overvoltage limit. The activation of the braking resistor is regulated through the PWM by comparing a carrier wave with the output of a proportional controller that is driven by the rise of V_c above 1930 V [31].

The line segment on the each side of the pantograph is depicted based on a LPL model [32] by using two cascaded identical π sections, as shown in Figure 6 where R_1, L_1 and C_1 (or R_2, L_2 and C_2) denoting the overall resistance, inductance and conductance of the left (or right) line segment, respectively, vary with the train position along the line section. Given the OHL parameters in Table 2 [24], the LPL model can approximately represent a maximum frequency range of around 74 kHz for a 1-km line segment [33]. Since the HRM generally focuses on system dynamics over a quite short period, the OHL segment can be assumed to have a fixed impedance in the HRM.

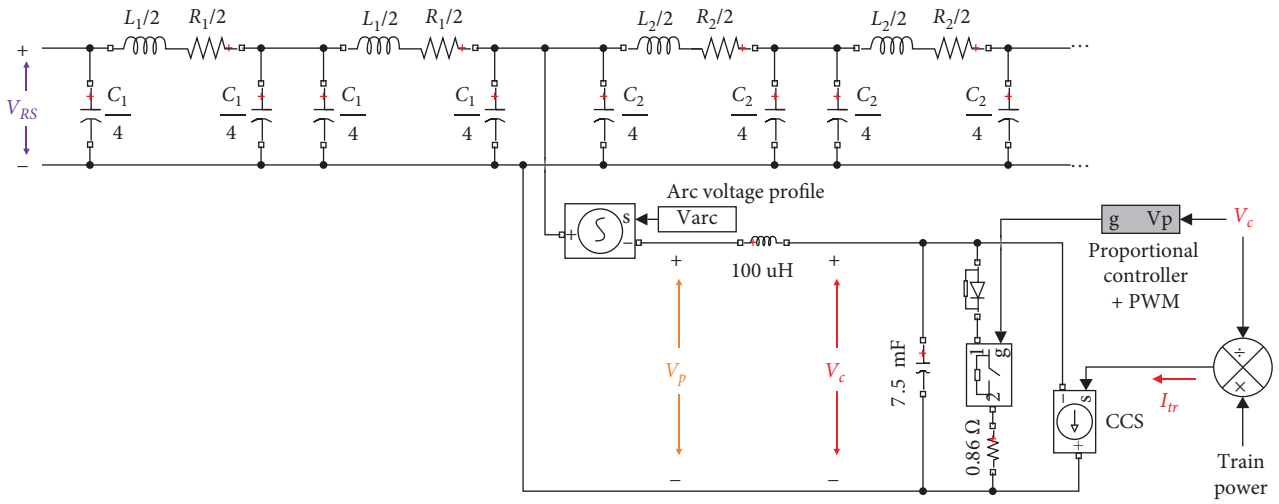

Figure 6: The circuit diagram of train and lumped parameter line models with insertion of arc voltage profiles at the pantograph.

Table 2: Technical parameters of the modelled OHL [24].

Parameter	Value
Resistance	0.17 Ω/km
Inductance	0.57 mΩ/km
Conductance	20 nF/km

2.4. Pantograph Arc Simulation. The pantograph-to-OHL contact force falling below a certain level will cause a contact loss and thus an undesired pantograph arc event, especially at the time of a heavy current flowing across the contact point [34]. The voltage distortion at the input stage of the train induced by pantograph arcing can propagate to an RS and interfere with power flows or even the operating mode of the RS. To assess impacts of pantograph arcing on the RS operation, a CVS is placed between the OHL and the train input to model the arc voltage V_{arc} occurring at the pantograph (Figure 6) [35], while the arc resistance in the order of 0.01–0.1 Ω [36] being small relative to the overall line impedance is usually neglected in the system simulation [37]. Figure 7 shows two approximate V_{arc} profiles which are extracted from the pantograph voltage V_p measured on a particular train within a 1.5 kV DC TPSS [38]. The positive or negative V_{arc} profile will be taken into the CVS in Figure 6 to model the arc event at the pantograph of an accelerating or braking train, respectively.

3. LRM of DC Traction System

3.1. Simplification of RS. In order to alleviate the computational burden in the long-term energy flow simulation, the modelling of the rectifier and the antiparallel VSI along with its constant DC voltage control is simplified in the LRM, as shown in Figure 8. The 12-pulse diode rectifier transformer is modelled by a series connection of a CVS and a diode which keeps the braking current from flowing across the rectifier. The CVS simulates the rectifier's output voltage V_{reco} that is correlated with the output current I_{reco} via its output characteristics as shown in Figure 9. The output characteristics are determined by measuring V_{reco} of the rectifier when it exports different levels of I_{reco}. The nonlinear output curve shows that V_{reco} rapidly decreases from the rectifier's no-load voltage when it starts to export current to the DC side [39] and then relatively slowly reduces with I_{reco} increasing further.

To reflect the reverse path enabled by the VSI under the constant DC voltage control as was detailed in Section 2.2, a DC voltage source of $V_{VSI,act}$ is placed in parallel with the CVS branch and managed by an ideal switch which is activated if $V_{RS} \geq V_{VSI,act}$, as shown in Figure 8. The DC V-I monitored at the RS can be employed to approximately estimate the power exchange P_{RS} between AC and DC sides via the RS by using Equation (5) where the positive or negative values of P_{RS} indicate the AC power supplied to or fed by the DC side, respectively:

$$P_{RS} = \begin{cases} V_{reco} \cdot I_{reco} / f_{A2D}(I_{reco}) \text{ for } I_{RS} \geq 0 \\ V_{VSI,act} \cdot I_{RS} \cdot f_{D2A}(I_{RS}) \text{ for } I_{RS} < 0 \end{cases}, \quad (5)$$

where $f_{A2D}(\cdot)$ or $f_{D2A}(\cdot)$ is the efficiency of the RS rectifying AC to DC or inverting DC to AC, respectively, inclusive of transformer losses. Since V_{reco} is dependent on I_{reco} and the VSI input voltage is constantly sustained at $V_{VSI,act}$ in the inverting mode, $f_{A2D}(\cdot)$ and $f_{D2A}(\cdot)$ can be described in terms of the rectifier's output current I_{reco} and the magnitude of VSI input current I_{RS}, respectively. Based on the power monitored at the main AC grid and at the DC side of the rectifier that exports a wide range of DC current, the conversion efficiency of the rectifier inclusive of transformer losses is calculated and paired with the corresponding DC current to obtain the efficiency curve, as shown in Figure 10a. The VSI's efficiency curve inclusive of transformer losses (Figure 10b) is determined in a similar way based on the power export to the main AC grid and the import into the VSI when it absorbs different levels of DC current.

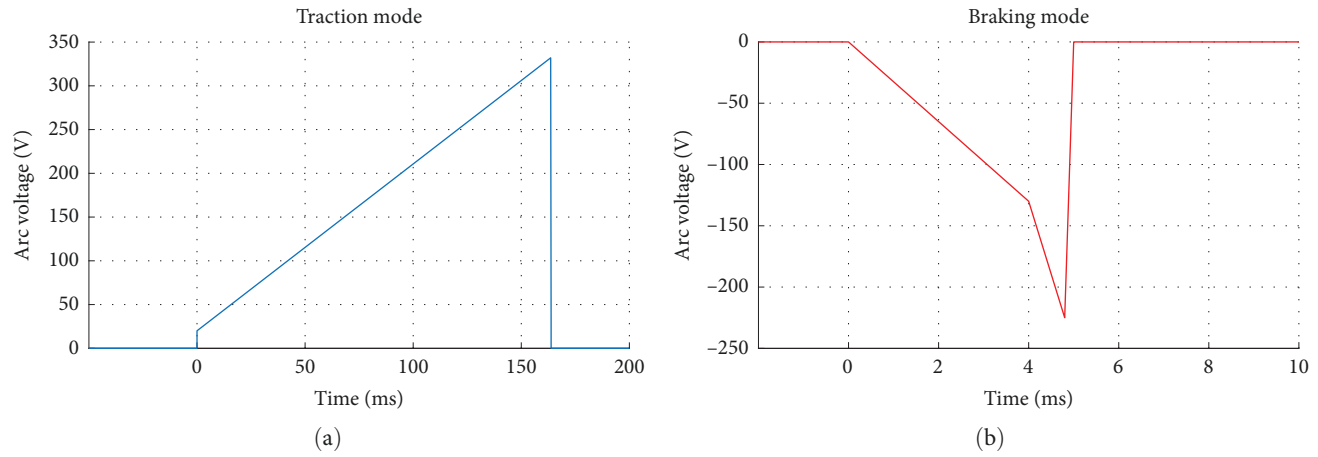

FIGURE 7: The voltage profile of the arc occurring at the pantograph of a particular train in the (a) traction or (b) braking mode in a 1.5 kV DC TPSS.

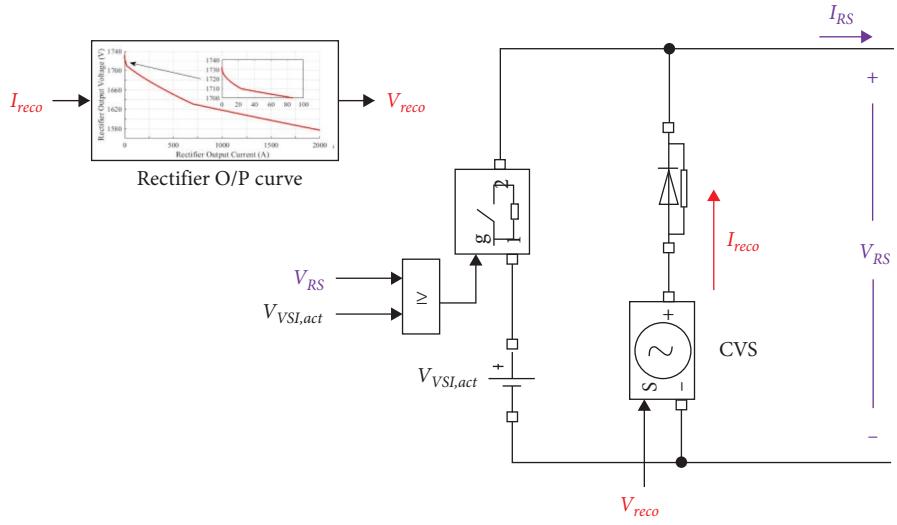

FIGURE 8: The simplified representation of converters at the RS in the LRM.

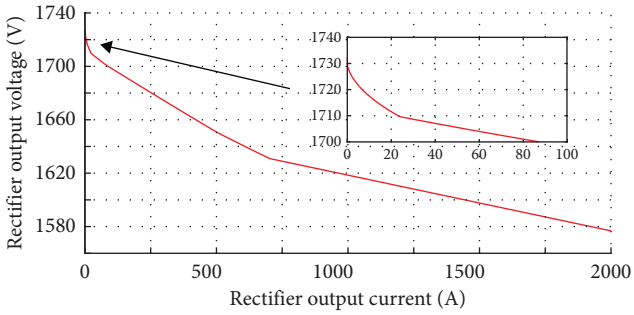

FIGURE 9: The nonlinear output curve of the modelled 12-pulse diode rectifier.

3.2. Variable Resistor Simulation. In the long-term energy flow simulation, the resistances of the OHL segments split by a train varying with the train movement cannot be ignored. Since the LRM dealing with the energy estimation does not require a high accuracy in the simulation of system transients, the LPL-based OHL segment in the HRM is replaced by a pure resistor line (PRL) in the LRM. The variable resistance of the OHL segment is estimated as the product of the OHL resistance per kilometre (Table 2) and the segment length. The estimated resistance value is then achieved in the LRM by switching on or off a cascade of series connected resistors which range from 1–4 Ω to 10–40 μΩ [5]. Figure 11 shows parts of the series connected resistors which can provide an accuracy of 10 μΩ. Through updating the train position and line segment resistances at each time step, the train movement along an OHL section is simulated by the LRM.

4. Results and Model Validation

The MRMs are developed here by using MATLAB/Simulink [40] based on a particular 1.5 kV TPSS which comprises an RS and four USs supplying the train operation between 11 stations along two opposite directions. A particular 15-s period is adopted for a case study where there are nine trains

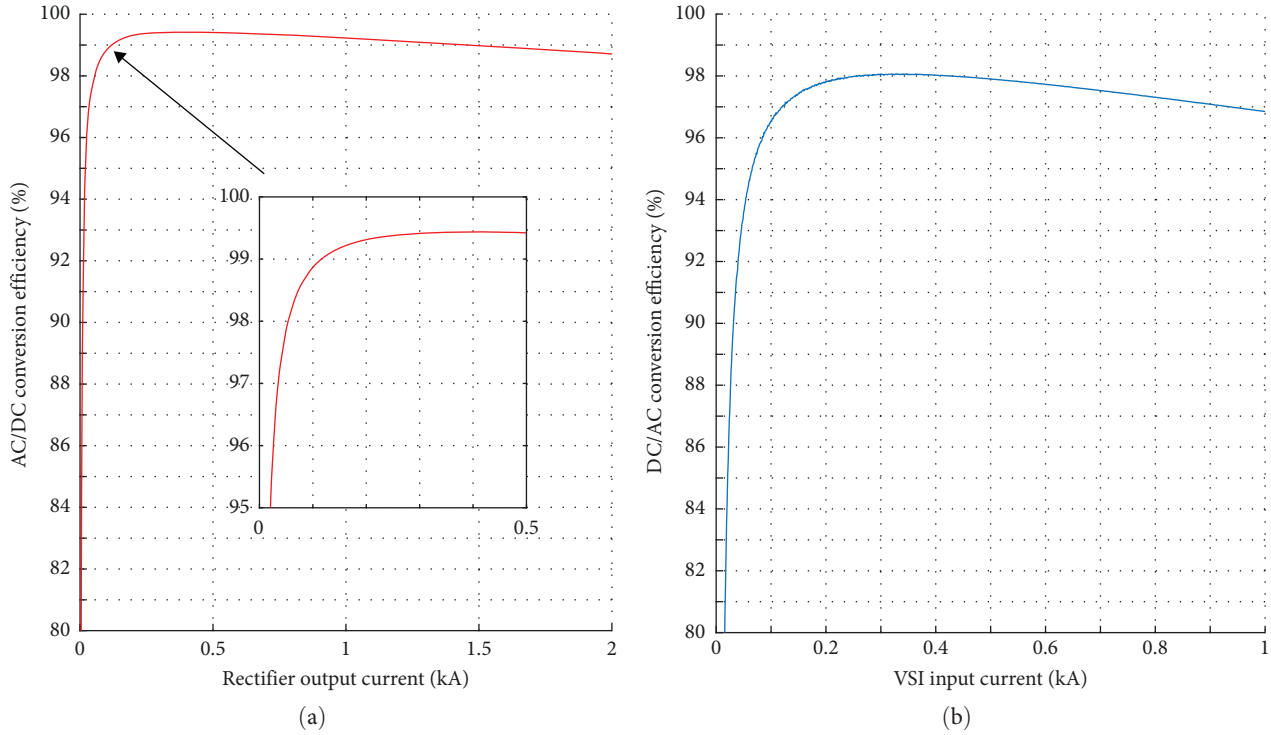

FIGURE 10: (a) The AC-to-DC and (b) DC-to-AC conversion efficiencies of the modelled D + VSI-based RS.

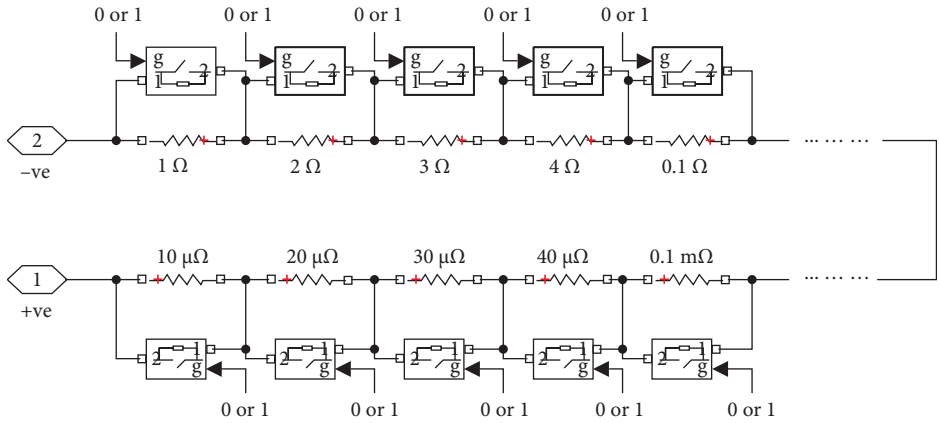

FIGURE 11: The variable resistance of an OHL segment simulated by a cascade of series connected resistors.

moving along tracks within the TPSS, as shown in Figure 12, which permits the MRMs to be tested in multiple train operation. The train positions along tracks in this period are inferred from a time–position diagram (Figure 13) that presumes trains to depart from the two starting stations (i.e. S1 and S11) in turn every 5 min. Figure 14 shows the time series of electrical power of each train computed from the on-board V-I measurements [30] during the 15-s period which sees a mixture of traction and braking modes of multiple trains.

Although the HRM running at a 5-μs time interval is suitable to the short-term simulation (≤1 s), it is used here to produce high-fidelity power flows over the 15-s period as a benchmark to assess the LRM accuracy in terms of the energy flow simulation. The LRM developed in Section 3 has been tested based on a range of time intervals from 5 μs to 1 s, from which a 0.1-ms interval is adopted to ensure the accuracy of the energy flow simulation while reducing the computation burden in the long-term simulation. The computation time used by the HRM or the LRM is about 13.6 or 1.1 min, respectively, i.e. nearly a 92% reduction in the LRM. (The computer being used has a 64-bit operating system, 192 GB of RAM and an Intel Core i9-10920x, 3.5 GHz processor.) In this section, the V-I dynamics at RS3 are simulated by the HRM first to investigate the RS3 operation under the normal train operation or pantograph arc events, followed by an assessment on the LRM's accuracy in the energy flow simulation and its application to the estimation of braking energy recovery efficiency. In addition, the technical performance of the two RS

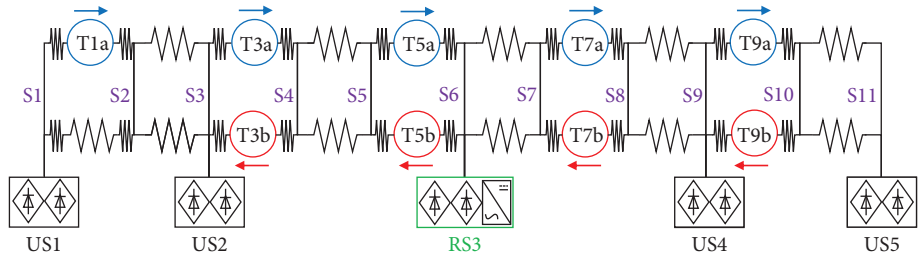

FIGURE 12: The diagram of a 1.5 kV DC TPSS comprising multiple trains (T) between 11 stations (S) supported by an RS and four USs over a particular 15-s period.

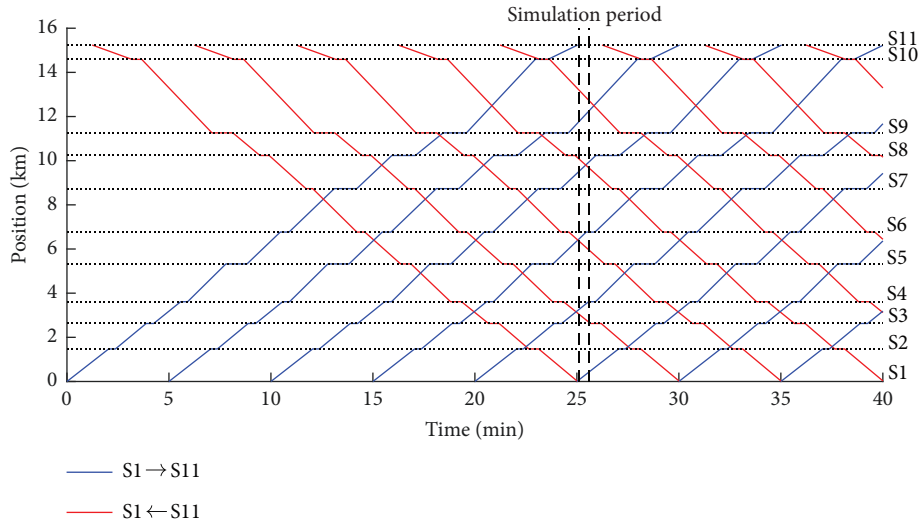

FIGURE 13: The time (min)–position (km) diagram of multiple trains within a 1.5 kV DC TPSS including the 15-s simulation period over 1520–1535 s.

topologies (Figures 1 and 2) is compared in V-I dynamics and energy flows that are simulated under normal operation.

4.1. V-I Transients at RS Under Normal Train Operation. The DC V-I dynamics at the D + VSI-based or VSC-only-based RS simulated by the HRM using LPL segments are shown in Figure 15. In the case of the D + VSI-based topology that connects diode rectifiers with an ANPC VSI, the 15-s simulation period can be divided into seven time slots, as indicated by the term *R*, *I* or *D* in Figure 15 which denotes the RS being in the rectifying mode, the inverting mode or the deadband, respectively. The RS is shown to operate according to the control method developed in Section 2: (i) the RS works in the rectifying mode when V_{RS} is smaller than the rectifier's no-load voltage of 1732.4 V; (ii) the RS starts to feed the braking current back to the AC side at around 1524.9 s when V_{RS} exceeds the VSI's activation voltage of 1780 V and then constantly maintains V_{RS} at around 1780 V; and (iii) it enters the deadband when I_{RS} rises to 0 at around 1530.7 s where the VSI is switched off and the rectifier is blocked due to V_{RS} still exceeding the no-load voltage. When the VSC-only-based RS that uses bidirectional ANPC VSCs is modelled, V_{RS} is shown to be always kept at around the no-load voltage of rectifiers at other USs, as was designed in Section 2. Furthermore, the RS is switched between rectifying and inverting modes without the transition of deadband.

Due to the existence of filter inductors and capacitors within the DC TPSS, some visible V-I oscillations are shown to occur at times of the train power changing stepwise. To examine the influences of LPL components on the V-I oscillations, the V-I dynamics at RS3 simulated by the HRM based on PRL segments are also shown in Figure 15. The enlarged graphs in Figure 15 illustrate that the LPL components increase the significance of V-I oscillations, which can be explained from the frequency domain of V-I signals. Figure 16 shows the spectra of I_{RS} simulated based on LPL and PRL models over 1530.5–1530.6 s or 1531.3–1531.4 s where RS3 is in the inverting or rectifying mode, respectively. The use of LPL segments causes a resonance at around 100 Hz which leads to larger and slower I_{RS} oscillations than the PRL-based I_{RS} in the time domain. In addition, the I_{RS} spectrum for the inverting mode shows a peak at 4 kHz which relates to the doubling of apparent switching frequency of the ANPC VSI (or VSCs), as was noted in Section 2.2. In the I_{RS} spectrum for the rectifying mode, the continuous use of the 12-pulse diode rectifiers at RS3 results in peaks at integer

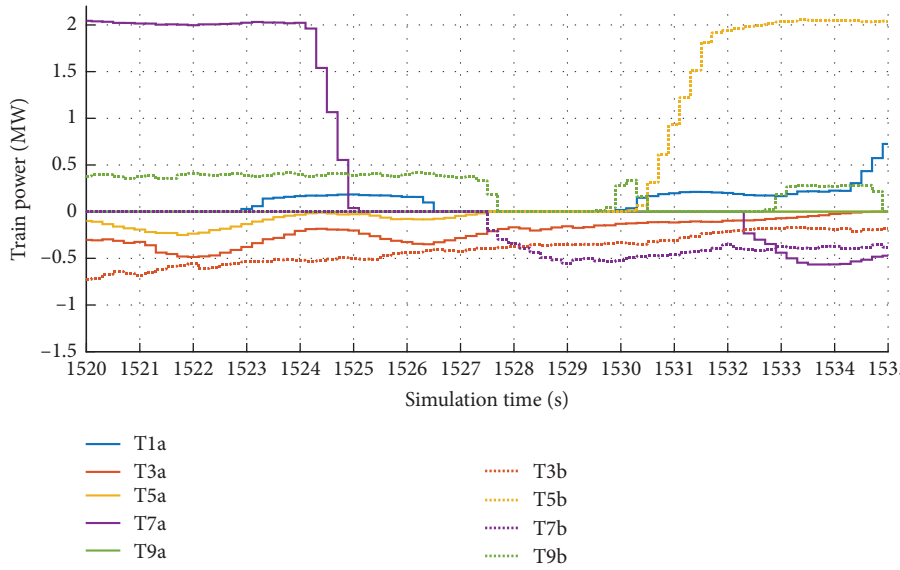

FIGURE 14: The 0.1-s average power (MW) of trains on tracks over the 15-s simulation period.

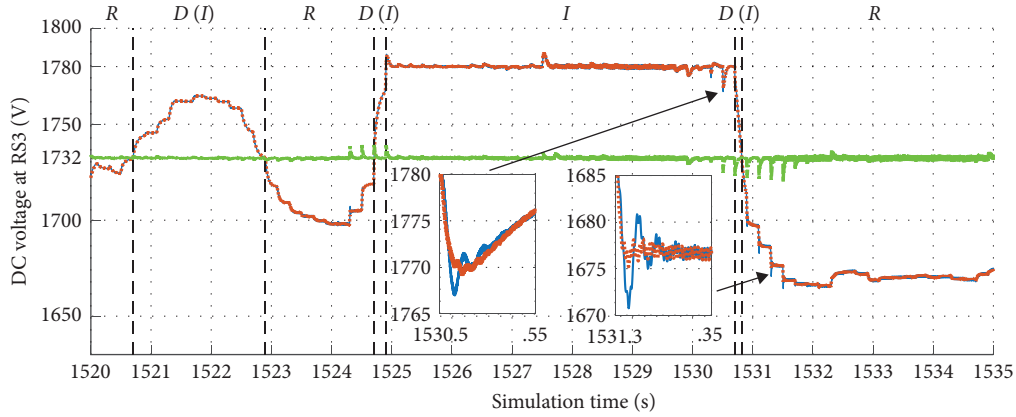

(a)

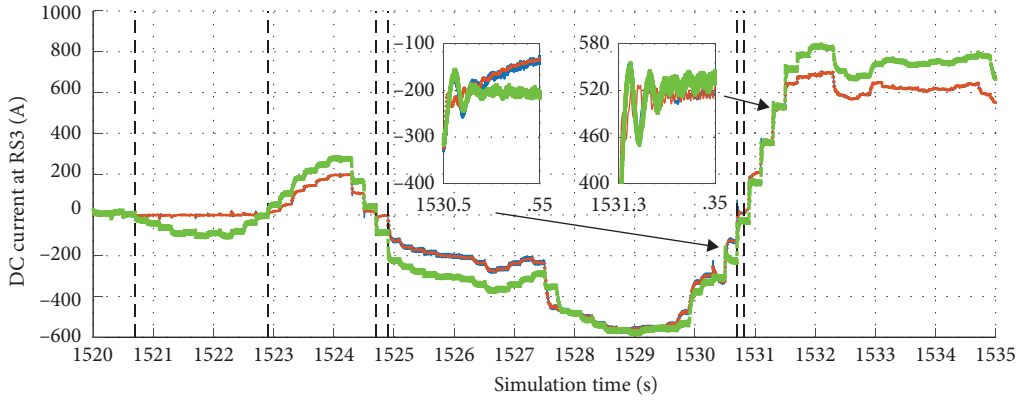

(b)

FIGURE 15: (a) DC voltage V_{RS} (V) and (b) current I_{RS} (A) at the D + VSI- or VSC-only-based RS modelled by the HRM using LPL or PRL segments over the 15-s simulation period.

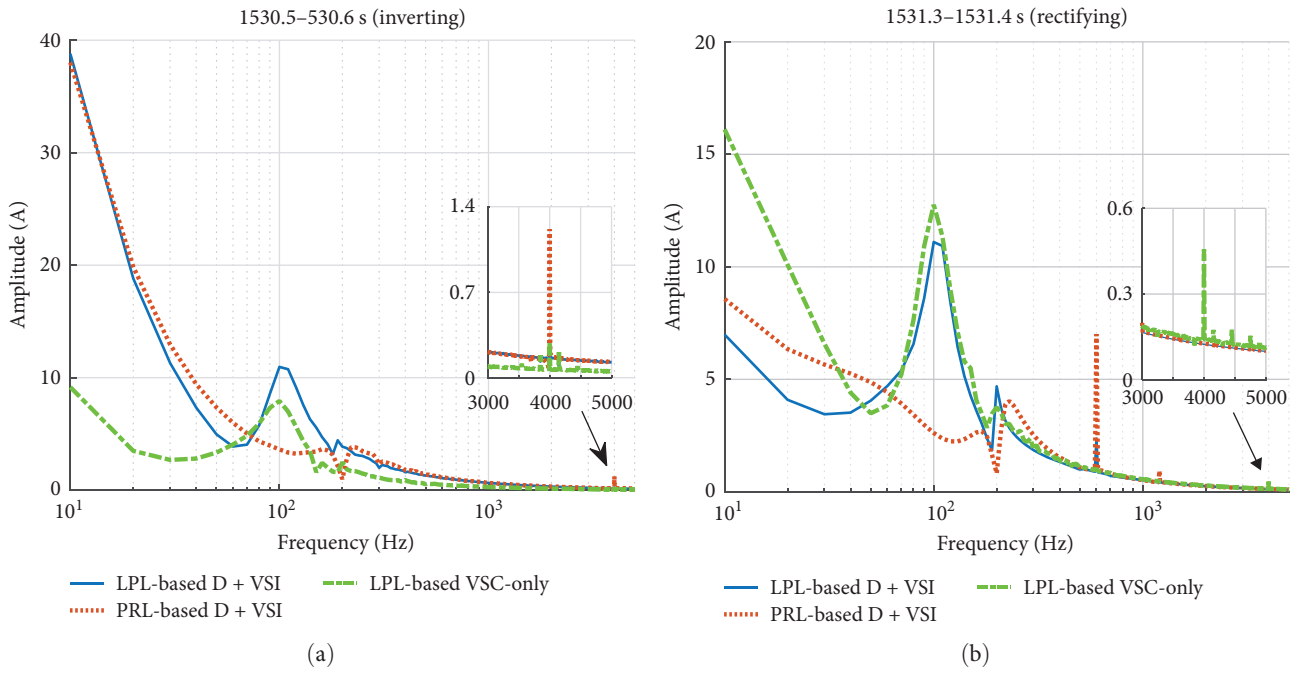

FIGURE 16: Frequency spectra of I_{RS} (A) at the D + VSI- or VSC-only-based RS simulated by the HRM using LPL or PRL segments (a) over 1530.5–1530.6 s in inverting mode and (b) over 1531.3–1531.4 s in rectifying mode.

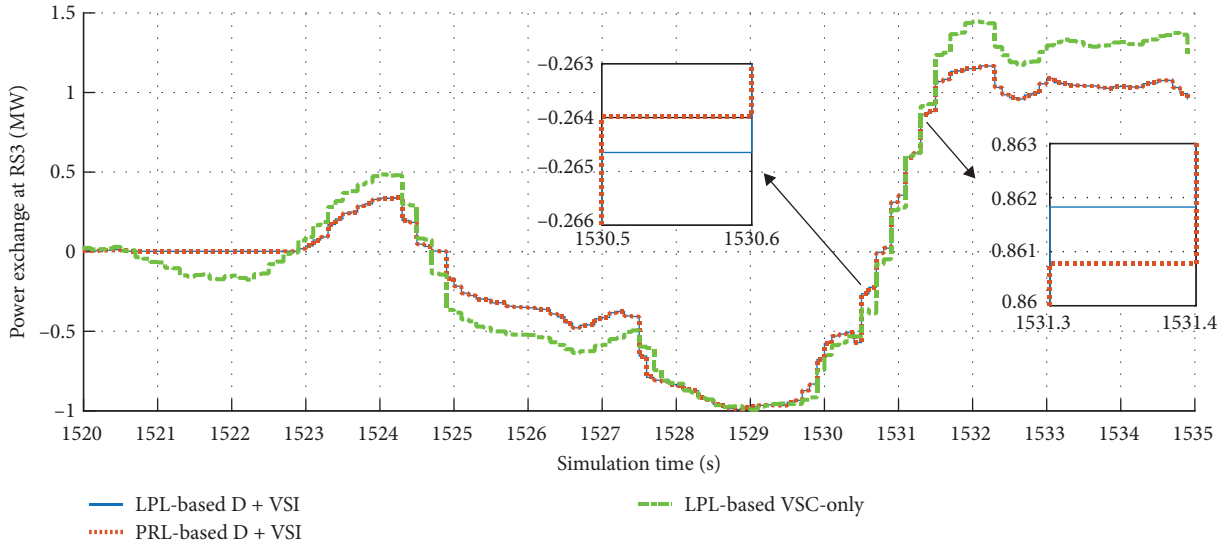

FIGURE 17: The 0.1-s average power exchange (MW) at the D + VSI- or VSC-only-based RS modelled by the HRM using LPL or PRL segments in the 15-s period.

multiples of the 12th harmonic of the nominal 50 Hz, while the entire replacement with bidirectional ANPC VSCs causes a peak at 4 kHz related to the apparent switching frequency.

In the case of the D + VSI-based RS topology, despite the existence of some slight differences between LPL- and PRL-based V-I transients, the use of LPL and PRL segments produces very similar simulations of power flows across RS3 on average over the 15-s period, as shown in Figure 17. This means that the employment of PRL segments in the LRM will contribute little to the overall simulation errors of energy flows. Figure 17 also shows the power flows across the VSC-only-based RS3 simulated based on LPL segments. Compared to the antiparallel VSI which is triggered at 1780 V, the bidirectional VSCs maintaining V_{RS} at 1732.4 V result in a higher system receptivity for braking energy and can feed more braking energy to the AC side (e.g. over 1524.9–1527.5 s), though this may occasionally mitigate the braking energy recovery by neighbouring trains.

4.2. Impacts of Pantograph Arcing on RS. A pantograph arc event with the positive or negative V_{arc} profile in Figure 7 is presumed to occur at the pantograph of the accelerating train T5b at 1532 s or the braking train T7b at 1529 s, respectively.

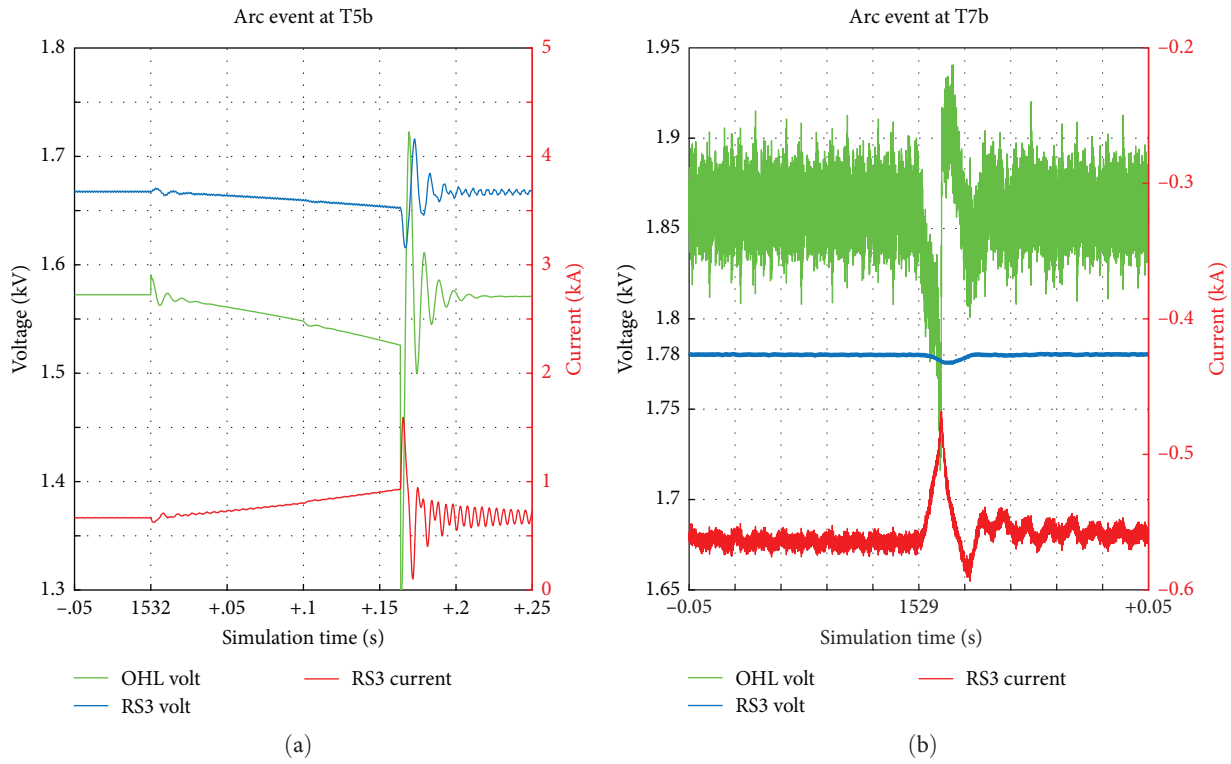

FIGURE 18: DC voltage (kV) and current (kA) at the D + VSI-based RS and line voltage (kV) at (a) the accelerating train T5b around 1532 s or (b) the braking train T7b around 1529 s in the presumed pantograph arc event.

The resulting OHL voltage waveform at the train position together with the V-I waveforms at the D + VSI-based RS is plotted in Figure 18. The line voltage disturbances are shown to (i) follow the V_{arc} profile with oscillations after the ignition and extinction of the pantograph arcing and then (ii) propagates to the RS, causing oscillations of V_{RS} and I_{RS}. Since V_{RS} always fluctuates below the rectifier's no-load voltage of 1732.4 V in Figure 18a and I_{RS} oscillations do not exceed zero in Figure 18b, the operating modes of the RS (i.e. rectifying in Figure 18a and inverting in Figure 18b) are not altered in the presumed arc events. However, it implies that the pantograph arcing may cause the RS moving into the deadband or even the opposite mode given a sufficient arc intensity.

Even though the pantograph arc events presumed here do not change the operating mode of the RS, they are found to reduce the energy efficiency of the TPSS, as shown in Figure 19a,b where the magnitudes of power import (or export) via the RS in the arc event are greater (or smaller) on average than in the normal operation. The drop of the RS export is also reflected in the three-phase current $I_g^{3\phi}$ fed by the RS. Figure 20a,b shows the AC current waveform along phase C during 1528.95–1529.05 s and its corresponding frequency spectrum, respectively, under the normal train operation or the arc event. The pantograph arcing not only reduces the AC current amplitudes but also increases the magnitudes of lower-order harmonics, degrading the quality of the braking power fed-to the AC side. It is noted that the phase current spectrum in Figure 20b comprises relatively larger harmonics at around 4 kHz, i.e. twice the switching frequency of the ANPC VSI. This is because the PWM strategy applied to the VSI leads to a natural doubling of the apparent switching frequency.

4.3. Energy Flow Simulation Accuracy of LRM. The energy exchanges at each US and the D + VSI-based RS modelled by the HRM are adopted here as the benchmark to assess the LRM accuracy in terms of the energy flow simulation. Figure 21 compares the power flows across US2, RS3 and US4 simulated by the two models. The LRM is shown to generate the 0.1-s average power flows similar to those of the HRM. Table 3 tabulates the energy import or export via each substation calculated by the two models. Compared to the HRM, the LRM overestimates the energy export at RS3 by around 0.8% and underestimates the import at most substations by less than 3%. It is noted that US1 and US2 witness more significant underestimation in energy import. This may be because the current flow across US1 or US2 is mostly smaller than 180 A (i.e. corresponding to around 0.3 MW), within which the rapidly rising AC-to-DC conversion efficiency estimate is less stable and relatively less precise than the efficiency calibrated for the high current levels (Figure 10a). However, since energy imports via US1 and US2 are lower than other traction substations, the percentage error of total TPSS import is about −0.4% only (Table 3).

4.4. Braking Energy Recovery in Multitrain Operation. Figure 22 shows the stacking of 0.1-s average power imports/exports at substations against the aggregate traction or braking power of trains when the D + VSI-based RS topology is modelled. In the 15-s simulation period, the overall energy regenerated by the braking trains is around 4.06 kWh,

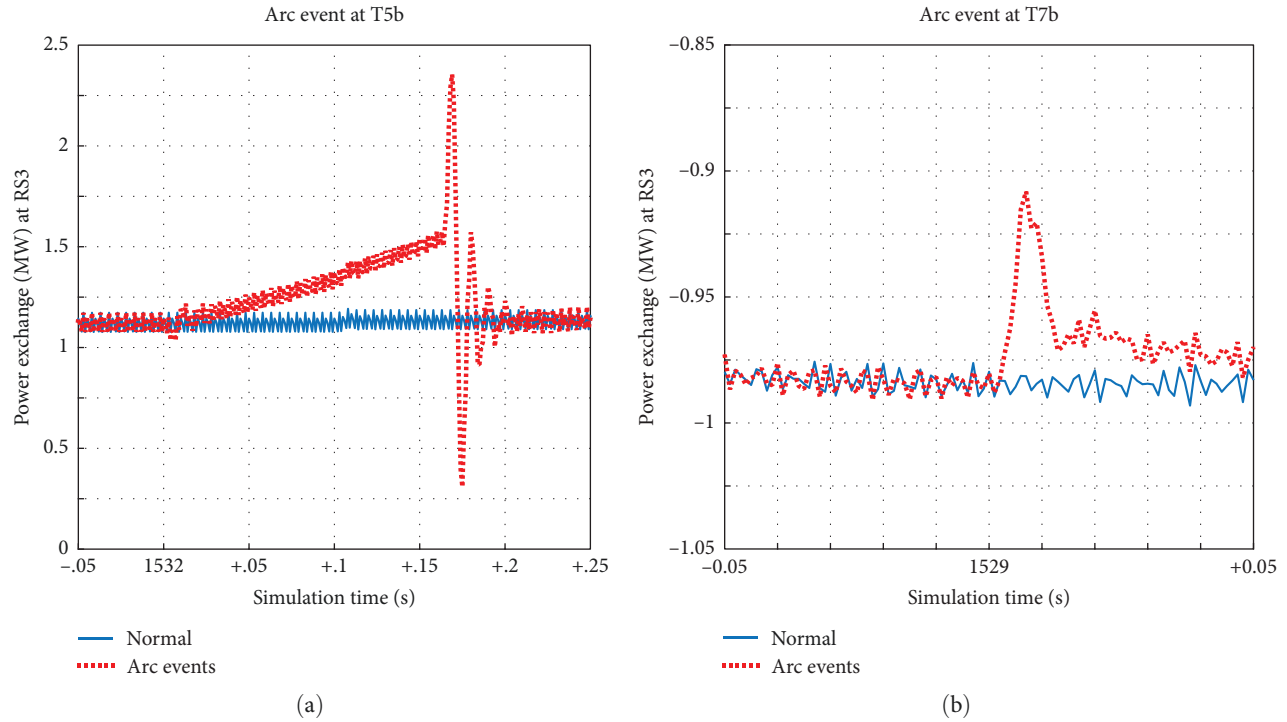

FIGURE 19: The 1-ms average power exchange (MW) at the D + VSI-based RS under the normal train operation or the presumed arc event around (a) 1532 s or (b) 1529 s.

23.8% of which (i.e. about 0.97 kWh) is recovered by RS3. Compared with the energy losses in RS3 and those along OHLs, most of the remaining braking energy is absorbed by the accelerating trains nearby. This is not only reflected by the large rise of the aggregate traction power of trains above the stacked substation import but also by the zero export of RS3 during the high braking power regeneration (e.g. over 1520–1524.9 and 1531–1535 s), as shown in Figure 22. It is evaluated that the overall energy consumption of trains is around 6.34 kWh which is 2.4 kWh greater than the total TPSS import (i.e. 3.94 kWh). This means that at least 2.4 kWh of braking energy (i.e. 59.1% of the total volume) is transferred to neighbouring trains for their usage. Therefore, the energy interchange between accelerating and decelerating trains makes more contribution to the braking energy recovery than the RS in this simulation period.

In the case of the VSC-only-based RS topology, the stacking of 0.1-s average power exchanges at substations and the aggregate traction or braking power of trains are shown in Figure 23. As was noted in Section 4.1, keeping V_{RS} at a lower voltage level (i.e. 1732.4 V for bidirectional VSCs compared to 1780 V for an antiparallel VSI) improves the system receptivity for braking energy. Therefore, during 1520.7–1522.7 and 1524.7–1527.4 s, the bidirectional VSCs feed more braking energy to the AC side than the antiparallel VSI, as shown in Figures 22 and 23. However, since part of the braking energy which would otherwise be absorbed by neighbouring trains is fed back to the AC side, US4 and US5 are shown to increase their imports in the same periods. In addition, compared to the D + VSI-based topology that uses existing diode rectifiers for electricity supply, the bidirectional VSCs maintain V_{RS} at the rectifier's no-load voltage in rectifying modes and thus increase the output voltage of rectifiers at USs, especially US2 and US4 that are closer to RS3. This decreases the power supply from adjacent USs and increases the import through RS3, e.g. during 1522.9–1524.6 and 1530.9–1535 s, as shown in Figures 22 and 23. It is evaluated that, during the 15-s simulation period, the total energy import of the TPSS from the upstream AC network is around 4158.03 Wh (i.e. 170.38 Wh greater than 3987.64 Wh in Table 3), and the braking energy fed to the AC side is around 1175.88 Wh (i.e. 210.13 Wh greater than 965.74 Wh in Table 3). Nevertheless, compared to the D + VSI-based topology, the adoption of the VSC-only-based topology is estimated to reduce the net energy import by 39.75 Wh during the 15-s period, mainly due to the increased system receptivity for braking energy.

5. Discussions

Given the capability and accuracy of the LRM in the energy flow simulation, it can be applied to estimate the energy usage or saving of the TPSS for a longer period of interest or in an entire day. According to the time–position diagram in Figure 13, the LRM can determine the OHL sections where trains are located and then switch on the train components in the corresponding OHL sections. This permits the modelling of trains moving across passenger stations within the TPSS in daily operation. The VSC-only-based RS topology can be also simplified to a DC voltage source in a similar way, with its conversion efficiency curves inclusive of transformer losses being evaluated for a wide range of DC currents in both directions. Based on the long-term

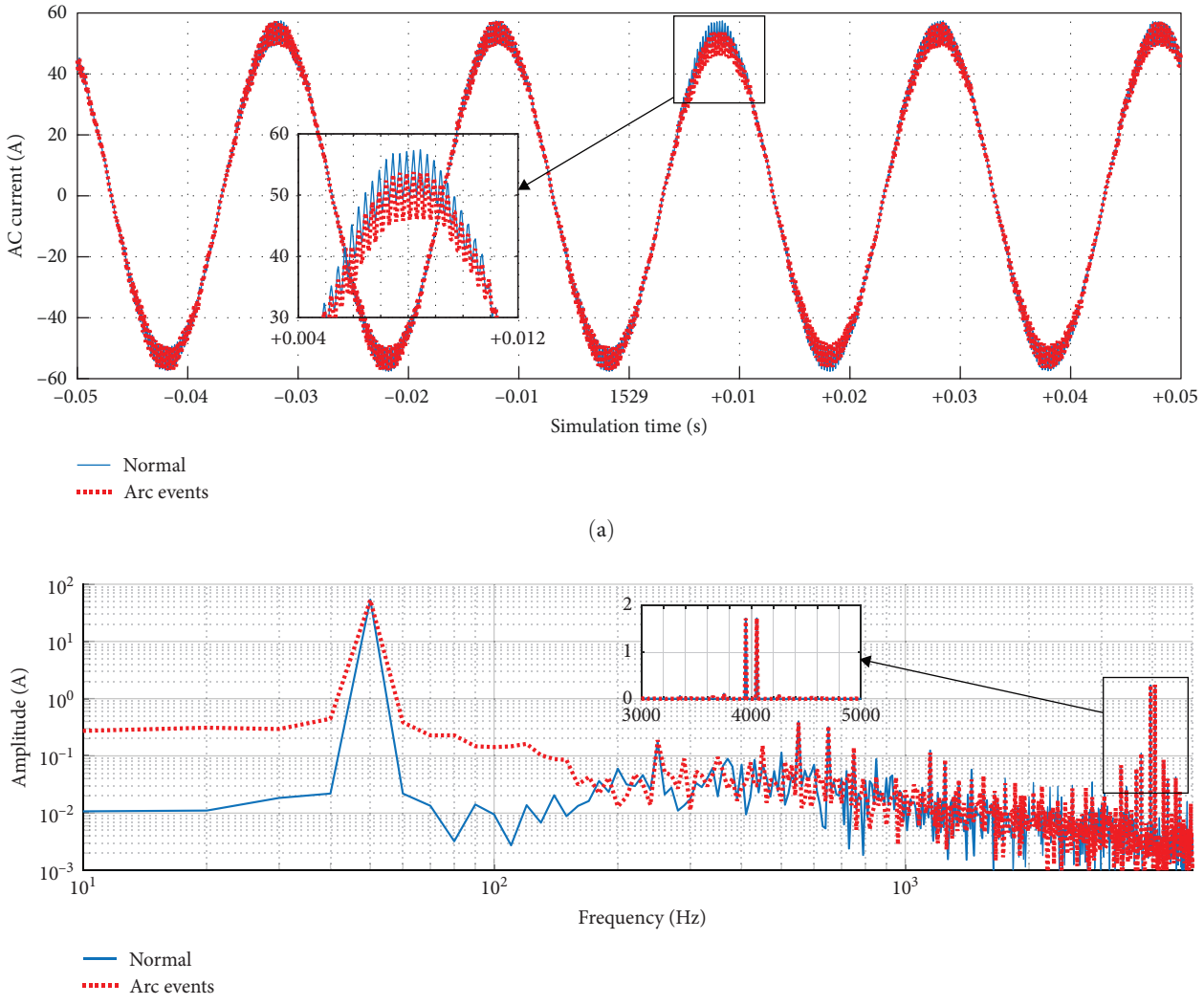

FIGURE 20: (a) The time series and (b) frequency spectrum of the AC current (A) along phase C fed by the D + VSI-based RS during 1528.95–1529.05 s under the normal train operation or the pantograph arc occurrence at T7b.

simulation of energy flows across a TPSS, the economics of operating the TPSS with or without a RS can be estimated to evaluate the economic benefits brought by the RS deployment, which can then be compared with the RS investment to determine the economic effectiveness. This will allow for an economic comparison between different RS topologies and facilitate the sizing of VSIs or VSCs for the RS. In this work, compared to the D + VSI-based topology where the VSI is used for braking energy recovery only, the entire replacement of rectifiers with VSCs in the VSC-only-based topology requires the VSCs to additionally transfer electricity from AC to DC for train consumptions, which generally has a greater peak than the braking energy fed-to the AC side (Figures 22 and 23). This will result in bidirectional VSCs requiring greater power capacities and thus increase the RS investment.

The braking energy dissipated in on-board braking rheostats, fed to the TPSS and recovered by the RS, can be calculated from system dynamics in the simulation. In practice, V-I monitoring devices are required to be installed at the locations of interest within the TPSS. For example, the typical places of V-I instrumentation within the input stage of a particular train is shown in Figure 24 [30], where the electricity consumption or the braking energy fed-to the OHL by the train can be estimated from measurements of V_p and I_p. However, it is noted that the commonly used on-board instrumentation generally works with a sampling rate of few tens of hertz and cannot suitably acquire the current flowing in braking rheostats (i.e. I_{BR1} and I_{BR2}) which has pulsed waveforms with high-frequency content [41]. While railway operators often prefer to estimate the wasted braking energy based on mechanical quantities subject to high uncertainties [41], some research has been devoted to correcting the V-I-based calculation by proposing a correction coefficient related to the duty cycle of the braking chopper [41, 42].

The regenerative braking energy that can be recovered and used through a RS varies depending on many factors, though an impact percentage ranging from 15% to 20% is

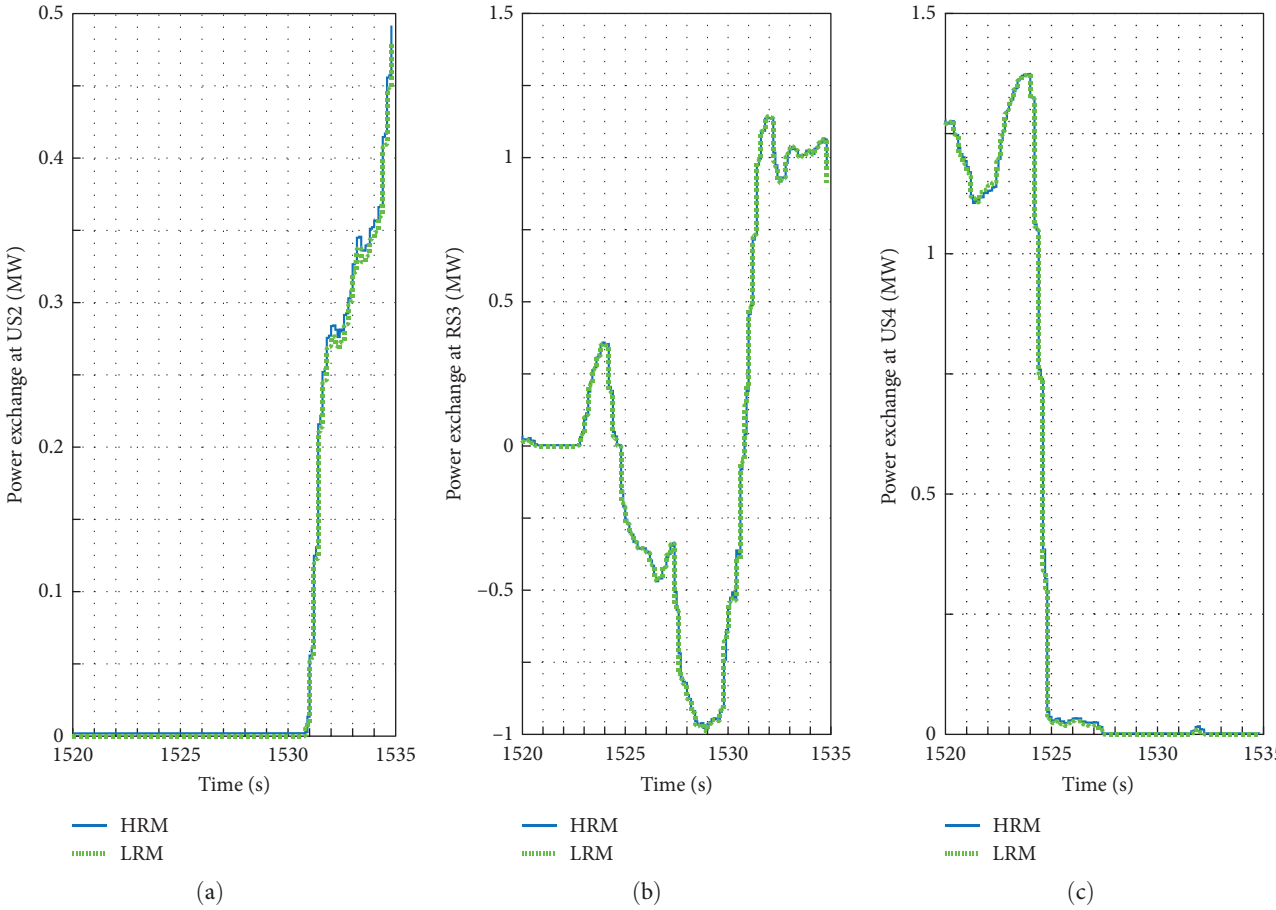

FIGURE 21: The 0.1-s average power exchange (MW) at (a) US2, (b) D + VSI-based RS3 and (c) US4 simulated by the HRM and the LRM over the 15-s period.

TABLE 3: Overall energy import/export via USs and D + VSI-based RS simulated by the MRMs in the 15-s period.

Substation	LRM (Wh)	HRM (Wh)	Error (Wh)	Error (%)
US1 import	260.08	265.76	−5.68	−2.14
US2 import	325.47	335.10	−9.63	−2.87
RS3 import	1188.51	1183.98	4.53	0.38
US4 import	1659.63	1656.47	3.16	0.02
US5 import	538.62	546.33	−7.71	−1.41
∑ import	3972.31	3987.64	−15.33	−0.38
RS3 export	−973.89	−965.74	−8.15	0.84

commonly adopted as the energy efficiency impact of a RS [43]. In addition to the system's receptivity for braking energy, the braking energy recovery of a RS is greatly affected by the number and locations of neighbouring trains which are generally prioritised to absorb regenerative braking energy in a natural way [44]. As was found in this work, more than half of the regenerated braking energy flows in neighbouring trains within the DC TPSS during the specific time period. Furthermore, the integration of regenerative braking energy into upstream AC networks is subjected to the legislations and rules of the AC networks which ensure the network safety and reliability (e.g. Engineering Recommendation G5 [45] that specifies the harmonic voltage distortion limit for the connection of harmonic sources to electrical networks in the UK). This incurs in the need of determining the suitable RS topology and location(s) as well as associated control methods (e.g. the trigger voltage of the VSI) so as to meet the safety and power quality requirements of trains, TPSS and upstream networks, which can be validated by using the HRM for all possible operating conditions before practical tests.

6. Conclusions and Future Work

This paper has developed MRMs to simulate the operation of a RS within a DC TPSS and assess its impacts on short-term system transients and long-term energy flows. A HRM focusing on short-term transient simulations replicates a particular RS topology where an ANPC VSI is antiparallel connected with 12-pulse diode rectifiers via the secondary winding of the existing rectifier transformer. To reduce the computation burden in long-term energy flow simulation, a LRM is further developed to simplify converter representations by using a CVS and a parallel DC voltage source to reflect the nonlinear output characteristic of the rectifier and the constant DC voltage control method applied to the VSI, respectively. In addition, the HRM or the LRM simulates OHL segments by LPL or PRL models, respectively, to ensure the fidelity of V-I

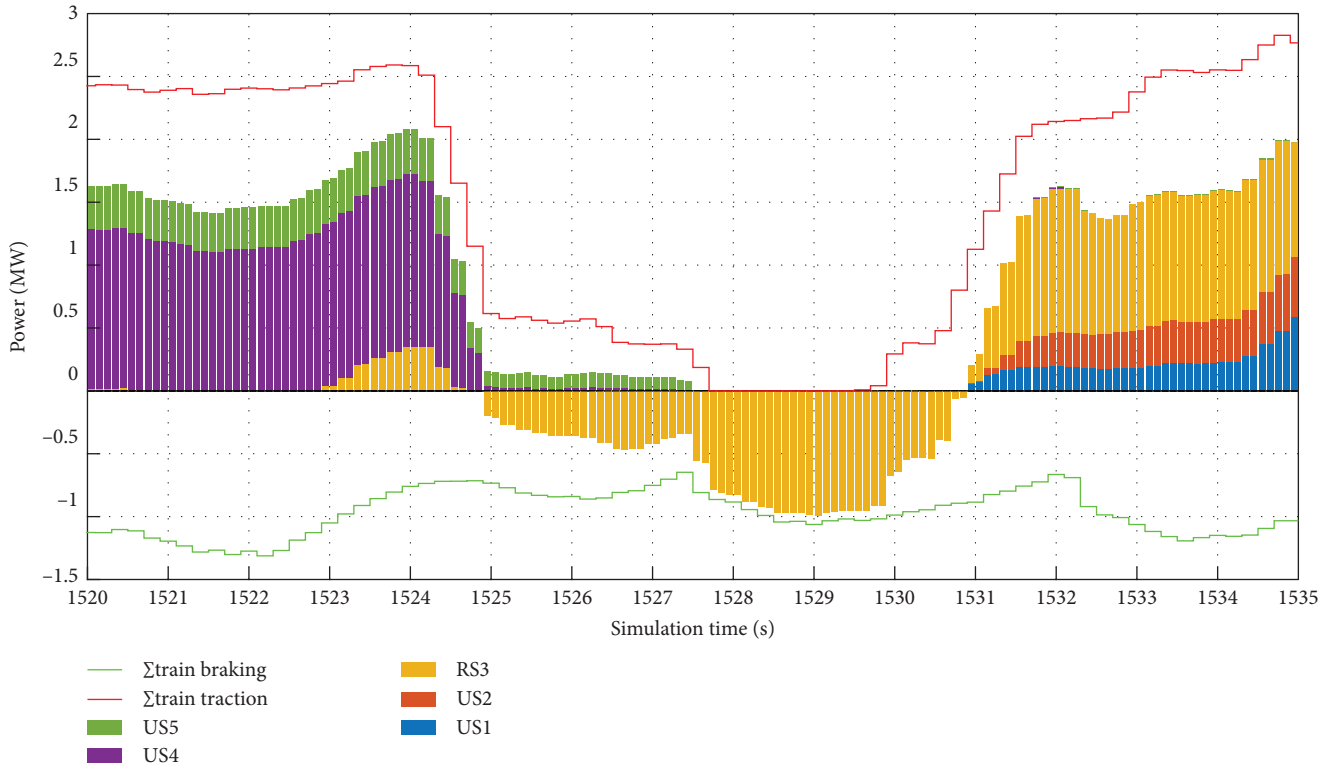

FIGURE 22: The stacking of 0.1-s average power flows (MW) at traction substations (with the D + VSI-based RS topology) and the aggregate traction or braking power (MW) of trains over the 15-s period.

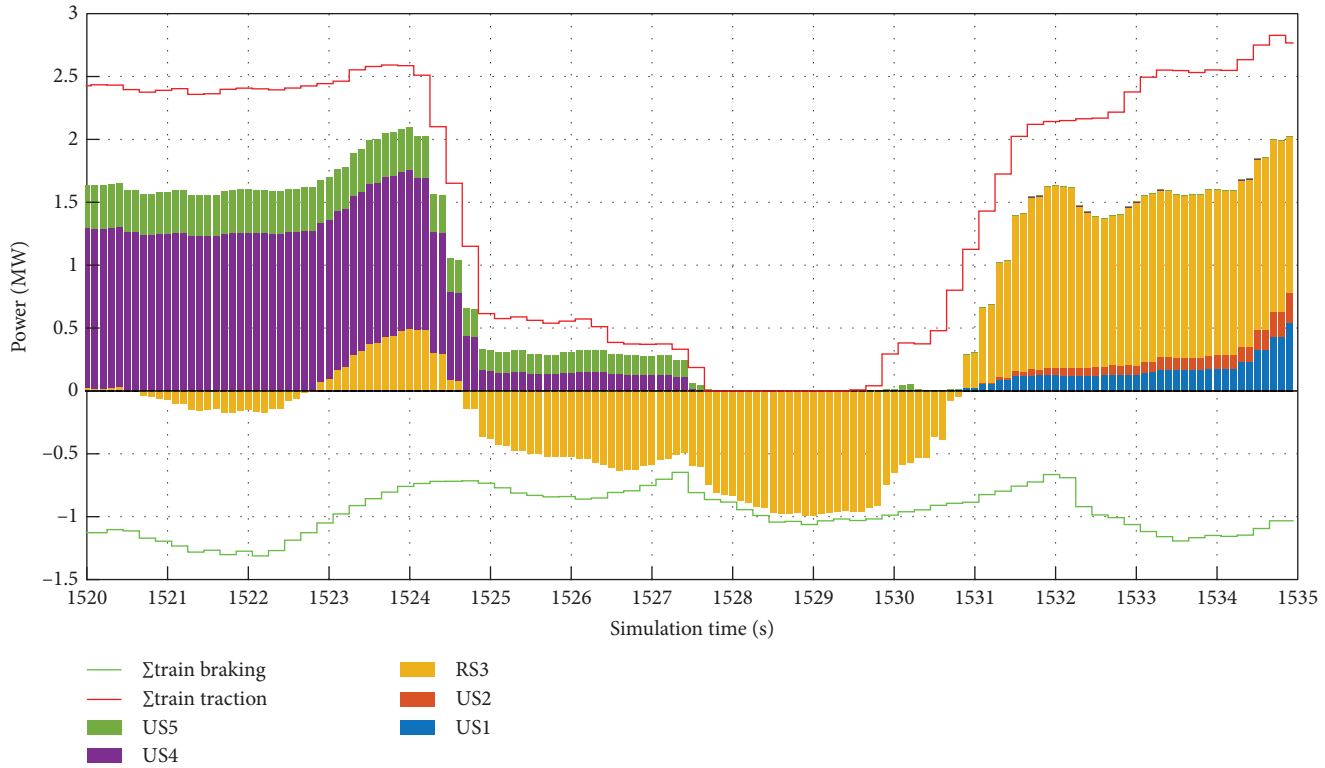

FIGURE 23: The stacking of 0.1-s average power flows (MW) at traction substations (with the VSC-only-based RS topology) and the aggregate traction or braking power (MW) of trains over the 15-s period.

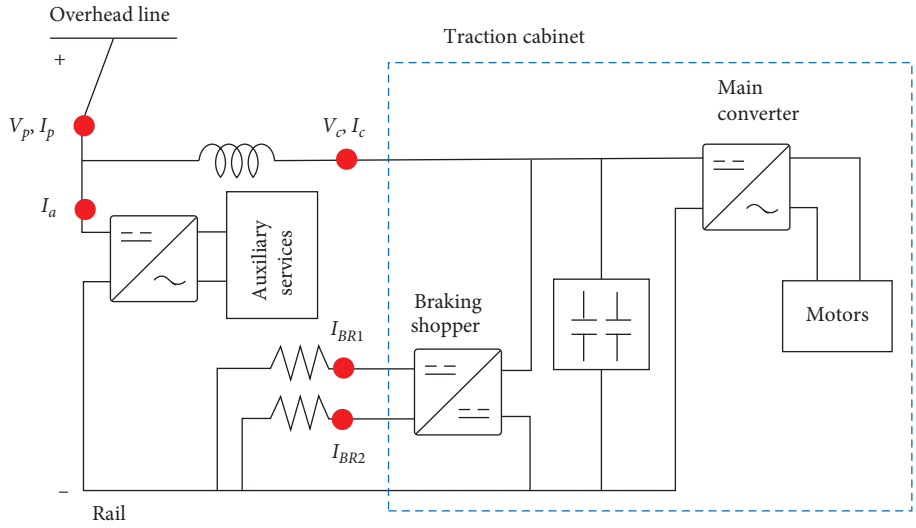

FIGURE 24: The schematic of the train input stage with V-I monitoring locations [30].

transients or permit updating OHL segment resistances with the train movement in long-term simulations. The HRM can also describe V-I transients at times of the pantograph arcing by placing a CVS between the train input and the OHL to model pantograph arc voltage profiles.

The MRMs have been tested based on a particular 1.5 kV DC TPSS which supports the multiple train operation by an RS and four USs. The V-I transients at the RS simulated by the HRM running at a 5-μs interval have shown that the RS operation follows the designed control method and that the use of LPL segments depicts the V-I oscillations more accurately than the PRL. Furthermore, the OHL voltage distortion induced by the pantograph arcing propagates to the RS, not only reducing the energy efficiency of the TPSS but also degrading the power quality of the braking power fed-to the AC side. The V-I oscillations after the ignition or extinction of the pantograph arcing also present a possibility of altering the RS operation mode. Compared to the HRM, the LRM running at a 0.1-ms interval saves 92% of computation time and shows good consistency in the energy flow simulation, with a percentage error of around 0.38% or 0.84% for the total TPSS import or export, respectively. The fast computational LRM permits the long-term energy flow simulation with a sufficient accuracy, based on which the braking power recovery efficiency of the RS can be assessed. In addition, the RS topology replacing diode rectifiers with bidirectional ANPC VSCs has been also simulated in this work for comparison. The VSCs are controlled to keep the DC voltage at the no-load voltage of rectifiers at other USs and switch between rectifying and inverting modes without a voltage deadband that is required by the antiparallel connected VSI. Although the net electricity import of the TPSS is more reduced by the VSCs in the period under test, the natural energy exchange between neighbouring trains has been slightly mitigated.

Building on the present work, the impacts of the pantograph arcing will be further investigated by introducing different arc intensities into the HRM. Furthermore, the LRM will be enhanced to consider the movement of trains across passenger stations and simulate daily TPSS operation for long-term techno-economic assessments. In addition, the control method designed here can be adapted for a specific practical RS regulation so as to validate the MRMs based on the field measurements. The rectifiers' output characteristics and the converters' efficiencies must also be calibrated to ensure the consistency of the MRMs in energy flow simulation.

Data Availability Statement

The data used to support the findings of this study are available from the corresponding author upon request.

Disclosure

This paper is an extended version of the conference paper "Reversible substation modelling with regenerative braking in DC traction power supply systems" presented at the 2021 IEEE Texas Power and Energy Conference.

Conflicts of Interest

The authors declare no conflicts of interest.

Funding

The research was funded in part by the EMPIR Programme cofinanced by the participating states and in part by the European Union's Horizon 2020 Research and Innovation Programme under grant 16ENG04 MyRailS.

Acknowledgments

Support for the work described in this paper is gratefully acknowledged by the partners of the MyRailS Project.

References

[1] International Union of Railways, *Moving Towards Sustainable Mobility: A Strategy for 2030 and Beyond for the European Railway Section* (International Union of Railways, Paris (France), 2012).

[2] M. Khodaparastan, A. A. Mohamed, and W. Brandauer, "Recuperation of Regenerative Braking Energy in Electric Rail Transit Systems," *IEEE Transactions on Intelligent Transportation Systems* 20, no. 8 (2019): 2831–2847.

[3] M. Popescu and A. Bitoleanu, "A Review of the Energy Efficiency Improvement in DC Railway Systems," *Energies* 12, no. 6 (2019): 1092.

[4] A. González-Gil, R. Palacin, and P. Batty, "Sustainable Urban Rail Systems: Strategies and Technologies for Optimal Management of Regenerative Braking Energy," *Energy Conversion and Management* 75 (2013): 374–388.

[5] F. Fan and B. G. Stewart, "Power Flow Simulation of DC Railway Power Supply Systems With Regenerative Braking," in *2020 IEEE 20th Mediterranean Electrotechnical Conference (MELECON)* (Palermo, Italy: IEEE, 2020), 16–18.

[6] F. Fan, Y. Li, S. Ziani, and B. G. Stewart, "Reversible Substation Modelling With Regenerative Braking in DC Traction Power Supply Systems," in *2021 IEEE Texas Power and Energy Conference (TPEC)* (College Station, TX, USA: IEEE, 2021), 1–6.

[7] P. Arboleya, B. Mohamed, and I. El-Sayed, "DC Railway Simulation including Controllable Power Electronic and Energy Storage Devices," *IEEE Transactions on Power Systems* 33, no. 5 (2018): 5319–5329.

[8] G. Zhang, Z. Tian, P. Tricoli, S. Hillmansen, Y. Wang, and Z. Liu, "Inverter Operating Characteristics Optimization for DC Traction Power Supply Systems," *IEEE Transactions on Vehicular Technology* 68, no. 4 (2019): 3400–3410.

[9] P. Arboleya, C. Mayet, A. Bouscayrol, B. Mohamed, P. Delarue, and I. El-Sayed, "Electrical Railway Dynamical Versus Static Models for Infrastructure Planning and Operation," *IEEE Transactions on Intelligent Transportation Systems* 23, no. 6 (2022): 5514–5525.

[10] V. A. Kleftakis and N. D. Hatziargyriou, "Optimal Control of Reversible Substations and Wayside Storage Devices for Voltage Stabilization and Energy Savings in Metro Railway Networks," *IEEE Transactions on Transportation Electrification* 5, no. 2 (2019): 515–523.

[11] G. Zhang, Z. Tian, P. Tricoli, S. Hillmansen, and Z. Liu, "A New Hybrid Simulation Integrating Transient-State and Steady-State Models for the Analysis of Reversible DC Traction Power Systems," *International Journal of Electrical Power & Energy Systems* 109 (2019): 9–19.

[12] Z. Tian, S. Hillmansen, C. Roberts, et al., "Energy Evaluation of the Power Network of a DC Railway System With Regenerating Trains," *IET Electrical Systems in Transportation* 6, no. 2 (2016): 41–49.

[13] T. Kulworawanichpong, "Multi-Train Modeling and Simulation Integrated With Traction Power Supply Solver Using Simplified Newton-Raphson Method," *Journal of Modern Transportation* 23, no. 4 (2015): 241–251.

[14] F. Hao, G. Zhang, J. Chen, Z. Liu, D. Xu, and Y. Wang, "Optimal Voltage Regulation and Power Sharing in Traction Power Systems With Reversible Converters," *IEEE Transactions on Power Systems* 35, no. 4 (2020): 2726–2735.

[15] D. Ramsey, T. Letrouve, A. Bouscayrol, and P. Delarue, "Comparison of Energy Recovery Solutions on a Suburban DC Railway System," *IEEE Transactions on Transportation Electrification* 7, no. 3 (2021): 1849–1857.

[16] P. Arboleya, B. Mohamed, and I. El-Sayed, "Off-Board and on-Board Energy Storage versus Reversible Substations in DC Railway Traction Systems," *IET Electrical Systems in Transportation* 10, no. 2 (2020): 185–195.

[17] T. Liang and V. Dinavahi, "Real-Time Device-Level Simulation of MMC-Based MVDC Traction Power System on MPSoC," *IEEE Transactions on Transportation Electrification* 4, no. 2 (2018): 626–641.

[18] M. Khodaparastan and A. Mohamed, "Modeling and Simulation of a Reversible Substation for Recuperation of Regenerative Braking Energy in Rail Transit Systems," in *2019 IEEE Transportation Electrification Conference and Expo (ITEC)* (Detroit, MI, USA: IEEE, 2019), 1–5.

[19] X. Yang, H. Hu, Y. Ge, S. Aatif, Z. He, and S. Gao, "An Improved Droop Control Strategy for VSC-Based MVDC Traction Power Supply System," *IEEE Transactions on Industry Applications* 54, no. 5 (2018): 5173–5186.

[20] Y. Krim, K. Almaksour, H. Caron, et al., "Comparative Study of Two Control Techniques of Regenerative Braking Power Recovering Inverter Based DC Railway Substation," in *Proceeding 2020 22nd European Conference on Power Electronics and Applications* (Lyon, France: IEEE, 2020), 1–9.

[21] G. Zhang, J. Qian, and X. Zhang, "Application of a High-Power Reversible Converter in a Hybrid Traction Power Supply System," *Applied Sciences* 7, no. 3 (2017): 282.

[22] G. Zhang, Z. Tian, H. Du, and Z. Liu, "A Novel Hybrid DC Traction Power Supply System Integrating PV and Reversible Converters," *Energies* 11, no. 7 (2018): 1661.

[23] M. Schweizer, T. Friedli, and J. W. Kolar, "Comparative Evaluation of Advanced Three-Phase Three-Level Inverter/Converter Topologies against Two-Level Systems," *IEEE Transactions on Industrial Electronics* 60, no. 12 (2013): 5515–5527.

[24] A. Mariscotti and P. Pozzobon, "Synthesis of Line Impedance Expressions for Railway Traction Systems," *IEEE Transactions on Vehicular Technology* 52, no. 2 (2003): 420–430.

[25] Z. Tian, G. Zhang, N. Zhao, S. Hillmansen, P. Tricoli, and C. Roberts, "Energy Evaluation for DC Railway Systems With Inverting Substations," in *2018 IEEE International Conference on Electrical Systems for Aircraft, Railway, Ship Propulsion and Road Vehicles & International Transportation Electrification Conference (ESARS-ITEC)* (Nottingham, UK: IEEE, 2019), 1–6.

[26] S. Z. Abbas, *Simulation, Implementation and Testing of Three-Phase Controlled Power Inverter Behaviour*, (Master's Thesis, (The Polytechnic University of Milan, Milan (Italy), 2016).

[27] S. Chattopadhyay, M. Mitra, and S. Sengupta, "Electric Power Quality," in *Clark and Part Transform*, (Springer, Dordrecht (Netherlands), 2011): 89–96.

[28] D. Floricau, E. Floricau, and M. Dumitrescu, "Natural Doubling of the Apparent Switching Frequency Using Three-Level ANPC Converter," in *2008 International School on Nonsinusoidal Currents and Compensation* (Lagow, Poland: IEEE, 2008), 1–6.

[29] M. Saleh, O. Dutta, Y. Esa, and A. Mohamed, "Quantitative Analysis of Regenerative Energy in Electric Rail Traction Systems," in *2017 IEEE Industry Applications Society Annual Meeting* (Cincinnati, OH: IEEE, 2017), 1–7.

[30] G. Cipolletta, A. D. Femine, D. Gallo, et al., "Monitoring a DC Train Supplied by a Reversible Substation," in *2020 IEEE International Instrumentation and Measurement Technology Conference (I2MTC)* (Dubrovnik, Croatia: IEEE, 2020), 1–6.

[31] Simulate an AC Motor Drive, (The MathWorks, Inc.; c1994-2022), 2023, Available from: https://uk.mathworks.com/help/physmod/sps/powersys/ug/simulating-an-ac-motor-drive.html#f4-7404.

[32] PI Section Line, "The MathWorks, Inc.; c1994-2022," 2023, https://uk.mathworks.com/help/physmod/sps/powersys/ref/pisectionline.html.
[33] N. R. Chaudhuri, B. Chaudhuri, R. Majumder, and A. Yazdani, *Multi-Terminal Direct-Current Grids, Modeling, Analysis, and Control* (Wiley, Hoboken (NJ), 2014): 87–89.
[34] S. Midya, D. Bormann, T. Schutte, and R. Thottappillil, "Pantograph Arcing in Electrified Railways—Mechanism and Influence of Various Parameters—Part I: With DC Traction Power Supply," *IEEE Transactions on Power Delivery* 24, no. 4 (2009): 1931–1939.
[35] F. Fan, A. Wank, Y. Seferi, and B. G. Stewart, "Pantograph Arc Location Estimation Using Resonant Frequencies in DC Railway Power Systems," *IEEE Transactions on Transportation Electrification* 7, no. 4 (2021): 3083–3095.
[36] G. Bucca and A. Collina, "A Procedure for the Wear Prediction of Collector Strip and Contact Wire in Pantograph-Catenary System," *Wear* 266, no. 1-2 (2009): 46–59.
[37] A. Mariscotti and D. Giordano, "Experimental Characterization of Pantograph Arcs and Transient Conducted Phenomena in DC Railways," *ACTA IMEKO* 9, no. 2 (2020): 10–17.
[38] D. Signorino, D. Giordano, A. Mariscotti, et al., "Dataset of Measured and Commented Pantograph Electric Arcs in DC Railways," *Data in Brief* 31 (2020): 105978.
[39] P. Pozzobon, "Transient and Steady-State Short-Circuit Currents in Rectifiers for DC Traction Supply," *IEEE Transactions on Vehicular Technology* 47, no. 4 (1998): 1390–1404.
[40] The MathWorks, Inc., *MATLAB Release* (The MathWorks, Inc., 2021).
[41] A. D. Femine, D. Signorino, D. Gallo, and D. Giordano, "A New Approach to Measure the Energy on-Board Train during Braking," *IEEE Transactions on Instrumentation and Measurement* 71 (2022): 9003411.
[42] D. Giordano, D. Signorino, D. Gallo, H. E. Van den Brom, and M. Sira, "Methodology for the Accurate Measurement of the Power Dissipated by Braking Rheostats," *Sensors* 20, no. 23 (2020): 6935.
[43] F. Cascetta, G. Cipolletta, A. D. Femine, et al., "Impact of a Reversible Substation on Energy Recovery Experienced on-Board a Train," *Measurement* 183 (2021): 109793.
[44] D. Cornic, "Efficient Recovery of Braking Energy through a Reversible DC Substation," in *Electrical Systems for Aircraft, Railway and Ship Propulsion* (Bologna, Italy: IEEE, 2010), 1–9.
[45] Engineering Recommendation G5 Issue 5, "Harmonic Voltage Distortion and the Connection of Harmonic Sources and/or Resonant Plant to Transmission Systems and Distribution Networks in the United Kingdom," (Energy Networks Association, London (UK) (2020).